JOURNAL OF SOLID STATE CHEMISTRY 115, 23–36 (1995)

A Single Crystal X-Ray Study of the Fluorite-Related "Solid Solutions" of CeO_2–$YO_{1.5}$

N. Gabbitas, J. G. Thompson,[1] R. L. Withers, and A. D. Rae

Research School of Chemistry, Australian National University, Canberra, Australian Capital Territory 0200, Australia

Received March 22, 1994; in revised form June 30, 1994; accepted July 1, 1994

A study of the $(1 - \delta)CeO_2 \cdot \delta YO_{1.5}$ solid solution has been undertaken to understand the origin of the two-phase region that occurs between the fluorite-type, 0–~50 mole% $YO_{1.5}$, and C-type, ~73–100 mole% $YO_{1.5}$, solid solutions. Single crystal X-ray diffraction data have been collected at 49.7, 73.0, and 79.8 mole% $YO_{1.5}$(cubic, $Ia\bar{3}$, a = 10.757(2), 10.698(4), 10.678(3) Å, Z = 32) and the structures refined to R_1 = 0.0841, 0.0146, and 0.0202 for 29, 25, and 72 independent reflections, respectively. The deviations from the ideal fluorite structure were examined and an apparent discontinuity observed for the metal atom shift allowed by $Ia\bar{3}$ symmetry. Previously suggested metal atom ordering was not observed in the C-type structure. Models have been proposed to understand the limiting compositions of the fluorite-type and C-type solid solutions. © 1995 Academic Press, Inc.

INTRODUCTION

The oxides of a variety of lower valent metals react with ZrO_2 or CeO_2 at high temperatures to give, upon quenching, "defect fluorite" type solid solutions. These typically exist over quite large composition ranges. In earlier papers on the ternaries $(1 - \delta)CeO_2 \cdot \delta RO_{1.5}$ (1–3) a continuous solid solution between the end members (fluorite-type for CeO_2 and C-type sesquioxide for $RO_{1.5}$) had been reported, but 25 years ago it was shown that there was a narrow two-phase region at approximately 60 mole% $RO_{1.5}$ (4, 5). The primary evidence for a continuous solid solution had been the appearance of C-type superlattice reflections of the form $G_F \pm 1/4\{220\}^*$ (where G_F refers to the strong Bragg reflections of the underlying fluorite-type average structure) in X-ray powder diffraction (XRD) patterns, starting (weak and diffuse) at about 10–20 mole% $RO_{1.5}$ and increasing in intensity and sharpness with increasing concentration of $RO_{1.5}$ The qualitative similarity of the reciprocal lattices of compositions on either side of the two-phase region can be seen in Fig. 1.

The presence of these apparent C-type superlattice reflections on the fluorite side of the two-phase region was originally interpreted as microdomains of essentially C-type structure embedded coherently into a fluorite matrix (4). Protracted annealing experiments between 1500 and 1700°C, however, showed that such systems could be reversibly moved from the "defect fluorite" or C-type region into the two-phase region and back again. This is not what would be expected for a "diphasic" texture of C-type domains dispersed in a fluorite matrix. Subsequently, Suzuki *et al.* (6–8) proposed an alternative explanation for the presence of these apparently C-type superlattice reflections in the $(1 - \delta)ZrO_2 \cdot \delta YO_{1.5}$ system in terms of condensed phonon modes independent of any oxygen vacancy ordering and involving only oxygen atom shifts. Thus the structural origin of the additional satellite reflections on either side of such two-phase regions remains unclear.

An earlier transmission election microscopy (TEM) study (9) confirmed two regions of homogenous solid solution, but found no evidence of a domain texture either via high resolution electron microscopy or satellite dark field imaging. All the evidence was consistent with variable amplitude commensurate modulation of an underlying average fluorite-type structure. In a concurrent paper (10) a modulated structure approach to the structural parameterization of any particular member of the CeO_2–$YO_{1.5}$ solid solution series was set out. It was shown that structure refinement involved the determination of compositional and displacement eigenvectors associated with two sets of modulation wave vectors–the first set being $1/4\{220\}_F^*$ type and the second being $1/2\{220\}_F^* \equiv \{001\}_F^*$ type. It was furthermore shown that oxygen vacancy ordering could only be associated with the primary $1/4\{220\}_F^*$ type modulations while metal atom ordering could only be associated with the second harmonic $\{001\}_F^*$ type modulations. The apparent disappearance of second harmonic $G_F + \{001\}_F^*$ type satellite reflections on the defect fluorite side (see Fig. 1a) suggested that the two-phase region at about 60 mole% $YO_{1.5}$ might be due to the sudden onset of compositional and/or displacive modulations associated with these second harmonic $\{001\}_F^*$ type modulation wave vectors.

[1] To whom correspondence should be addressed.

0022-4596/95 $6.00

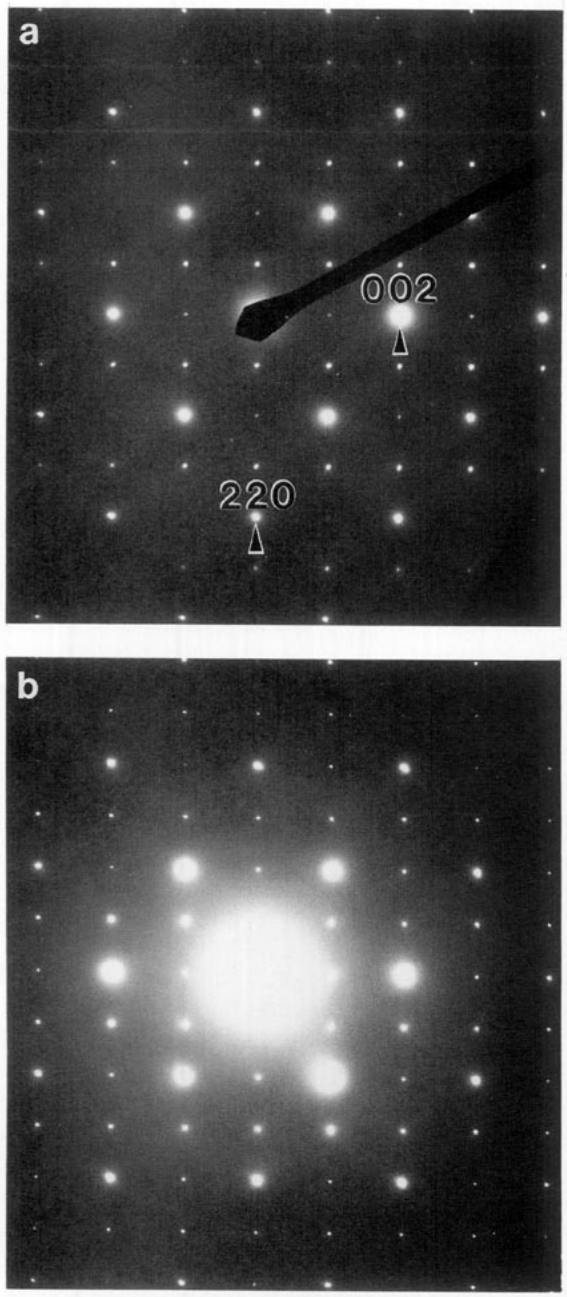

FIG. 1. Shows (110) type zone axis electron diffraction patterns for (a) 49.7 mole% and (b) 79.8 mole% $YO_{1.5}$ specimens. Labeling is with respect to the fluorite-type subcell.

As no previous single crystal structure refinements have been reported within either solid solution, apart from the end members, we have grown single crystal specimens on either side of the two-phase region and carried out structure refinements, with a view to determining the nature of the distortions responsible for the additional satellite reflections as well as to understanding the origin of the two-phase region. Space group symmetry $Ia\bar{3}$ ($a_{\text{C-type}} \sim 2 \times a_{\text{fluorite}} \sim 10.6$ Å) has been used and is consistent with previously reported TEM and XRD results on either side of the two-phase region. The CeO_2–$YO_{1.5}$ system has been chosen for study rather than ZrO_2–$LnO_{1.5}$ systems (in which similar phenomena occur), because the former system displays sharper satellite reflections and its lower melting point enables single crystal specimens to be grown more easily. Nevertheless any explanation of the origin of the two-phase region should also be applicable to ZrO_2–$LnO_{1.5}$ systems.

EXPERIMENTAL

Crystal Growth and Selection

Specimens were prepared on either side of and within the two-phase region at 49.7, 57.9, 64.8, 73.0 and 79.8 mole% $YO_{1.5}$. The 49.7 mole% $YO_{1.5}$ specimen was in the so-called fluorite-type solid solution and the 79.8 mole% $YO_{1.5}$ specimen in the C-type solid solution. The 64.8 mole% $YO_{1.5}$ was grown within the two-phase region in the hope of obtaining a single crystal specimen of either end member as the result of compositional unmixing and to determine the boundaries of the two-phase region. Specimens 57.9 and 73.0 mole% $YO_{1.5}$ were expected to occur on either side of the two-phase region, but subsequently proved to consist of two phases. However the 73 mole% $YO_{1.5}$ specimen was sufficiently close to the two-phase region boundary that, to a good approximation, it was single phase.

The component oxides CeO_2 and Y_2O_3 were thoroughly mixed mechanically, before being pressed into pellets. The pellets were placed on platinum foil supported by alumina, and annealed at 1600°C for a period of 7–10 days. Fragments of the well-sintered pellets were then melted in an arc furnace with argon as the ionizing medium, and again annealed for 7–10 days at 1600°C. Finally, samples were heated at 1000°C to reoxidize any Ce atoms which had been reduced to Ce^{III} during the high temperature melting and annealing steps. The success of this reoxidation was evident in the change in color of the specimens. Bulk specimens were characterized using XRD and unit cell dimensions determined using Guinier–Hägg data.

Crystal selection was made after examination of oscillation photographs obtained using a Weissenberg camera of arbitrarily oriented 60–100 μm crystal fragments. The fragments were of irregular shape with no discernible faces. Oscillation photographs often showed either multiple sets of Bragg reflections, corresponding to a mosaic of smaller domains slightly misoriented, or a dominant set with pronounced streaking at constant θ. Crystals which most closely resembled single domains were used.

Composition and Microstructure Analysis

Scanning electron microscopy (SEM) was performed with a JEOL 6400 microscope equipped with a Link Si

detector, Moran Scientific analyzer, and a Robinson backscattered electron detector for compositional analysis. Samples were carbon coated prior to analysis. Possible iron impurity was less than the limit of detection (~0.15 wt%). Backscattered electron micrographs were recorded using a Cambridge 360 scanning electron microscope also equipped with a Robinson detector.

Quantitative analyses of the $(1 - \delta)CeO_2 \cdot \delta YO_{1.5}$ specimens were carried out in a Cameca Camebax electron microprobe using energy dispersive spectroscopy (EDS) with reference standards of pure CeO_2 and Y_2O_3. Millimeter-sized fragments of the samples from which the single crystals were obtained were embedded in resin blocks, polished to a micrometer finish, and then carbon coated. Compositional analyses were obtained from volumes of ~1 μm^3 using a focused incident beam from a variety of sites on the samples.

XRD and TEM Analysis

X-ray powder diffraction (XRD) data of bulk specimens were collected with a Guinier–Hägg camera using monochromated Cu$K\alpha_1$ radiation. An internal standard of ThO_2 was used to determine accurately the cell parameter. The XRD data were converted to digital form for use in Fig. 2 using an Optronics P-1700 film scanner.

A JEOL 100CX transmission electron microscope was used to obtain electron diffraction patterns. Specimens were finely ground in a mortar and pestle then dispersed on a holey carbon grid.

Single Crystal Data Collection

Single crystal data were collected using a Philips PW1100/20 X-ray diffractometer (Mo$K\bar{\alpha}$ radiation, λ = 0.71069 Å) equipped with a graphite monochromator. Lattice parameters derived from the single crystals for the cubic system $Ia\bar{3}$ (T_h^7, No. 206) were determined from least-squares analysis of the setting angles of strong reflections (Note: in what follows reflection indexation is with respect to the $a_c = 2a_F$, $Ia\bar{3}$ C-type unit cell.) For the 49.7 mole% $YO_{1.5}$ crystal 13 reflections with $6.5° < 2\theta < 10.9°$ consisting of {222}, {400}, and {440} reflections; for the 73.0 mole% $YO_{1.5}$ crystal 23 reflections with $6.5° < 2\theta < 12.8°$ consisting of {222}, {400}, {440}, and {622} reflections and for the 79.8 mole% $YO_{1.5}$ crystal 25 reflections between $10.8° < 2\theta < 15.5°$ consisting of {440}, {622}, and {800} reflections were used.

The intensities of the full sphere $\pm h$, $\pm k$, $\pm l$ ($-10 \le h, k, l \le 10$, $2\theta < 39.68°$ for the 79.8 mole%; $-8 \le h, k, l \le 8$, $2\theta < 33.92°$ for the 49.7 and 73.0 mole%) were collected using ω-2θ scans of width $(1.00 + 0.346 \tan \theta)°$ in ω at a rate of 1.5° min^{-1} in ω with background counts of 25 sec on each side. Standard {222} reflections were measured every 90 min (except for the 73.0 mole% $YO_{1.5}$ specimen every 240 min) and showed no decomposition.

Data reduction to process the raw counts to h, k, l, F, and $\sigma(F)$, and application of a Lorentz–polarization and spherical absorption correction was carried out using Xtal3.2 (11). Due to poor crystal shape a spherical absorption correction was applied to the 49.7 and 79.8 mole% $YO_{1.5}$ data using radii of 0.1 and 0.2 mm, respectively. For the 73.0 mole% $YO_{1.5}$ data this correction was not applied. For all data sets an empirical absorption correction was applied during the refinement (see Single Crystal Refinement Results).

Structure Refinement

Structure refinement was achieved using RAELS92 (12). Atomic scattering factors, anomalous dispersion, and absorption coefficents are taken from the International Tables for X-Ray Crystallography (13). Data were initially (before the data merge) segmented according to information content: as parent fluorite-type reflections (h, k, l: $h + k = 4n$, $h + l = 4n$ and $k + l = 4n$), first harmonic reflections (h, k, l: h or k or l odd) or second harmonic reflections (h, k, l: h and k and l even or zero, but not a parent reflection). The second harmonics were further subdivided into those with h, k, and $l \neq 0$ and those with h, k, or $l = 0$ as metal atom ordering information is potentially most directly obtainable from this latter subset. Subsequently data with $I(h) > 3\sigma(I(h))$ were further segmented according to the proportion of equivalents observed: $\ge 1/2$, 1/4 – 1/2, 1/6 – 1/4, and <1/6, while retaining the distinction between parent, first harmonic, and second harmonic reflections. These categories were monitored to see whether the data subsets calculated on scale. Consequently, data subsets with only a few observed equivalents and which calculated low were excluded from the refinement. Exclusion of these unreliable data did not have a significant effect on the refined atomic parameters, but did result in a marked improvement in the refinement statistics as well as a small reduction in standard deviations.

STRUCTURAL DEGREES OF FREEDOM

Over most of the composition range from CeO_2 to $YO_{1.5}$, i.e., above about 30 mole% $YO_{1.5}$, the reflections observed conform to the $Ia\bar{3}$, $a_C = 2a_F$, space group symmetry of the Y_2O_3 structure. For Y_2O_3 itself, the occupied atom sites are as follows:

8Y(1)	in 8(*b*)	$(1/4\ 1/4\ 1/4)_C$
24Y(2)	in 24(*d*)	$(x\ 0\ 1/4)_C$

with $x = -0.0314$,

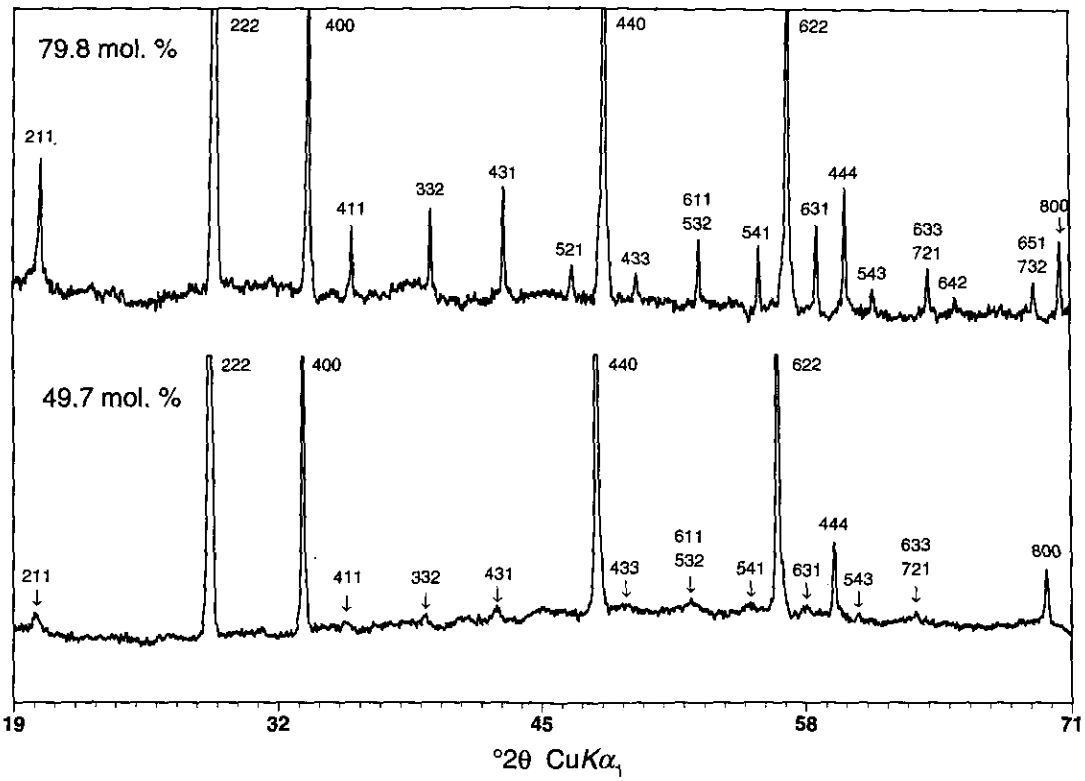

FIG. 2. Densitometer traces of XRD patterns (Cu$K\alpha_1$, λ = 1.5406 Å) for the 79.8 mole% (upper) and 49.7 mole% (lower) $YO_{1.5}$ specimens. The strong data have been truncated at ~15% of the {222} reflection to enhance visibility of the weaker satellite reflections. Note the striking reduction in intensity of the satellite reflections from the 79.8 mole% $YO_{1.5}$ specimen in the C-type solid solution to the 49.7 mole% $YO_{1.5}$ specimen in the fluorite-type solid solution. The satellite reflections in the latter specimen show significant peak broadening, indicating a reduced domain size. A single second harmonic reflection, $\{642\}_C$, can be seen for the C-type specimen at 65.4° 2θ.

and 48O(1) in 48(*e*)

$$(x, y, z)_C = (3/8 + \Delta O(1)_x,\ 1/8 + \Delta O(1)_y,\ 3/8 + \Delta O(1)z)_C$$

with the 16(*c*) site at

$$(x\,x\,x)_C = (1/8 + \Delta O(2)_x,\ 1/8 + \Delta O(2)_y,\ 1/8 + \Delta O(2)_z)_C$$

being unoccupied. The formula can be rewritten as $Ce_{(1-\delta)}Y_\delta O_{(1.5+0.5(1-\delta))}$, $Z = 32$, such that as CeO_2 is substituted for $YO_{1.5}$, the additional $16(1-\delta)$ oxygens occupy the 16(*c*), or O(2), site. For the compositions described herein,

$$\delta = 0.5, \quad 16(1-\delta) = 8$$
$$\delta = 0.73, \quad 16(1-\delta) = 4.32$$
$$\delta = 0.8, \quad 16(1-\delta) = 3.2.$$

The substitution of CeO_2 for $YO_{1.5}$ also gives rise to the possibility of metal atom ordering between the 8(*b*) and 24(*d*) sites. Hereafter the metal atom sites at $(1/4\ 1/4\ 1/4)_C$ and $(x\ 0\ 1/4)_C$ are referred to as R(1) and R(2), respectively.

Group Theoretical Considerations

As shown in Withers *et al.* (10), $Ia\bar{3}$ space group symmetry constrains compositional and/or displacive modulation waves associated with the primary $1/4\{220\}^*_F$ type modulation waves to transform with either Γ_2 or Γ_3 symmetry and the second harmonic $\{001\}^*_F$ type modulation waves to transform with Γ_{1g} symmetry. (Note, however, that oxygen vacancy ordering and consequent displacive relaxation can only be associated with the primary $1/4\{220\}^*_F$ type modulation waves which transform with Γ_2 symmetry).

The form of the $Ia\bar{3}$ space group symmetry allowed compositional and displacement eigenvectors associated with each of the observed modulation wave vectors was listed in Table 3 of Withers *et al.* (10). During the course of this work, however, it became apparent that one additional structural degree of freedom, the displacive degree of freedom associated with the primary $1/4\{220\}^*_F$ type modulation waves and of Γ_3 symmetry, had been ne-

TABLE 1
Compositional and Displacement Eigenvectors Associated with $1/4\{220\}_F^*$ Type Modulation Waves and Γ_3 Symmetry

	q_1 $1/4(02\bar{2})$	q_2 $1/4(2\bar{2}0)$	q_3 $1/4(\bar{2}02)$	q_4 $1/4(022)$	q_5 $1/4(220)$	q_6 $1/4(202)$
$\varepsilon_{O(1)x}$	0	ε_O'''	ε_O'''	0	ε_O'''	ε_O'''
$\phi_{O(1)x}$		0°	90°		90°	0°
$\varepsilon_{O(1)y}$	ε_O'''	ε_O'''	0	ε_O'''	ε_O'''	0
$\phi_{O(1)y}$	−90°	0°		180°	−90°	
$\varepsilon_{O(1)z}$	ε_O'''	0	ε_O'''	ε_O'''	0	ε_O'''
$\phi_{O(1)z}$	−90°		90°	0°		180°

Note. The parameters α_R, $\alpha_{O(1)}$, $\alpha_{O(2)}$, ε_{Rx}, ε_{Ry}, and ε_{Rz} are all zero for wave vectors q_1 to q_6.

glected. Table 1 gives the form of the corresponding $Ia\bar{3}$ space group symmetry allowed displacement eigenvectors using the same notation as Table 3 in (10). In terms of these modulation wave parameters, the $Ia\bar{3}$ space group allowed positions and occupancies (occ.) are given by

$$\Delta R(1) = 0 \qquad \text{occ.} = \bar{f}_R(1 + 3\alpha_R)$$
$$\Delta R(2)_x = -\varepsilon_R \qquad \text{occ.} = \bar{f}_R(1 - \alpha_R)$$
$$\Delta O(1)_x = 1/2(-\varepsilon_0 + 2\varepsilon_0' - \varepsilon_0'')$$
$$\Delta O(1)_y = 1/2(\varepsilon_0 + 2\varepsilon_0' + \varepsilon_0'')$$
$$\Delta O(1)_z = 1/2(\varepsilon_0 - \varepsilon_0'' - 2\varepsilon_0''') \qquad \text{occ.} = \bar{f}_0(1 + \alpha_0)$$
$$\Delta O(2)_x = 1/2(-\varepsilon_0 - 2\varepsilon_0''') \qquad \text{occ.} = \bar{f}_0(1 - 3\alpha_0).$$

As described previously (10), $\bar{f}_R$ and $\bar{f}_O$ represent average metal and oxygen site occupancies when referred to the underlying fluorite-type average structure. The remaining parameters represent the $Ia\bar{3}$ space group symmetry-allowed compositional (α_R and α_O) and displacive (ε_R, ε_O, ε_O', ε_O'', and ε_O''') modulation wave amplitudes associated with the primary $1/4\{220\}_F^*$ type and second harmonic $\{001\}_F^*$ type modulation waves. Note that we might expect only those displacive degrees of freedom associated with oxygen vacancy ordering, i.e., ε_R, ε_O, and ε_O' to have substantial magnitude (see Table 7) whereas those displacive degrees of freedom that do not have a compositional driving force, i.e., ε_O''' might be expected to refine to close to zero.

STRUCTURAL AND COMPOSITIONAL ANALYSIS

XRD

Guinier–Hägg data were indexed to a cubic unit cell with the cubic unit cell parameter being refined using a least-squares fit. The 79.8 mole% $YO_{1.5}$ was single phase with a unit cell parameter a_C = 10.674(13) Å and likewise the 49.7 mole% $YO_{1.5}$ was also single phase with $a_C = 2a_F$ = 10.765(19) Å. The 64.8 mole% $YO_{1.5}$ gave two distinct phases with a_C = 10.701(20) and 10.761(10) Å. These unit cell parameters were compared to the data of Bevan and Summerville (14) to give compositions of 48.1 mole% $YO_{1.5}$ for the theoretical 49.7 mole% $YO_{1.5}$ sample and 79.8 mole% $YO_{1.5}$ for the theoretical 79.8 mole% $YO_{1.5}$ sample. Based on the 64.8 mole% $YO_{1.5}$ specimen, we observed that the two-phase region occurs between 49.6 and 73.3 mole% $YO_{1.5}$ for our specimens. Figure 2 shows the densitometer traces of the films for the 79.8 and 49.7 mole% $YO_{1.5}$ specimens. Note the striking differences in intensity and half width of equivalent satellite reflections between the two compositions.

TEM

At any composition other than $\delta = 0$ or $\delta = 1$, partial occupancy of the O(2) 16(*c*) site is necessarily involved. The distribution of the $16(1 - \delta)$ oxygens available onto the 16 potentially available O(2) sites and the subsequent structural relaxation gives rise to a diffuse intensity distribution characteristic of the local short-range ordering involved.

Over-exposed electron diffraction patterns were therefore taken on either side of the two-phase region to look for any abrupt change in the character of this short-range ordering which might be associated with crossing over the two-phase region. Experimentally, however, the characteristic diffuse distributions on either side of the two-phase region appear, qualitatively, to be remarkably similar, as shown in Fig. 3.

Sample Homogeneity

Backscattered electron images of the diphasic region specimens showed that unmixing of the two compositions had only occurred on the micrometer scale. In the backscattered electron image, intensity is proportional to the average atomic number $\bar{Z}$. The darker, lower $\bar{Z}$ regions are the yttrium rich phase and the lighter, higher $\bar{Z}$ regions are the yttrium poor phase. Figure 4 shows an image of the 64.8 mole% $YO_{1.5}$ specimen in which the dark regions are yttrium rich ~73 mole% $YO_{1.5}$ and the light regions are cerium rich, yttrium poor ~50 mole% $YO_{1.5}$. Domains of mostly ~73 mole% $YO_{1.5}$ exist within the matrix of ~50 mole% $YO_{1.5}$. This was typical of the images although occasionally larger domains of up to 20 × 100 μm were observed.

Initially it was thought that unmixing occurred on a much larger scale (>100 μm) and hence it would be possible to obtain both end members of the two-phase region (~50 and ~73 mole% $YO_{1.5}$) from the single specimen. In fact, it was possible to obtain "apparent" single crystals from the 64.8 mole% $YO_{1.5}$ sample, as determined by

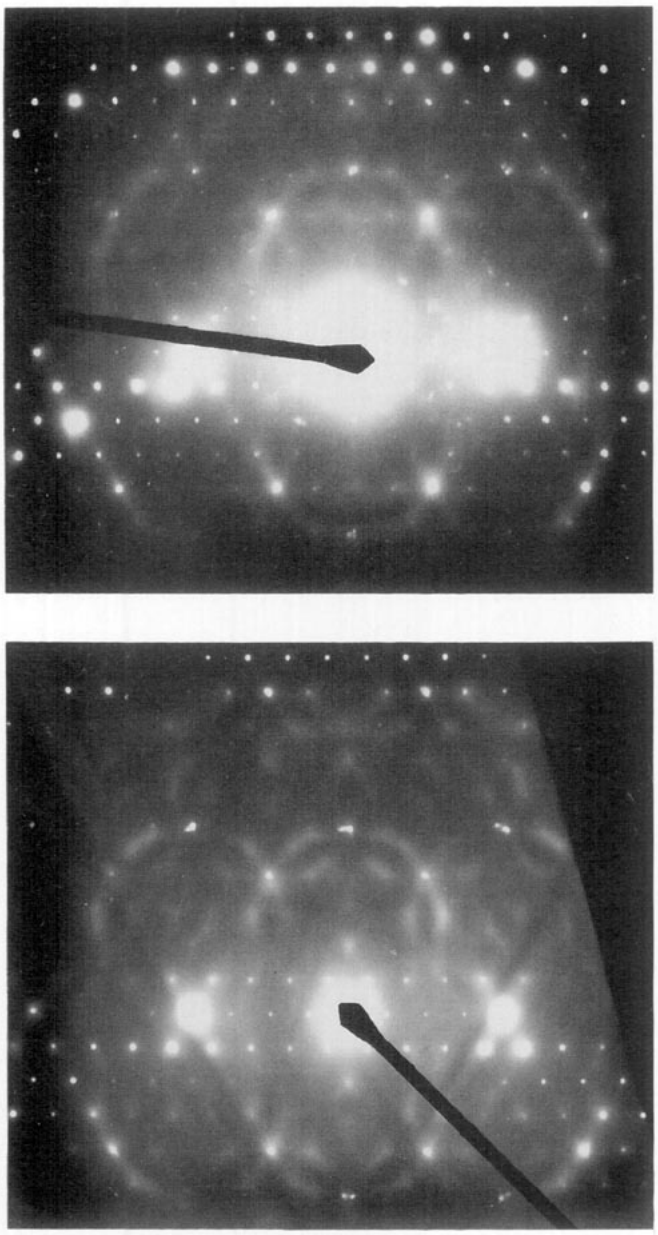

FIG. 3. Shows selected area electron diffraction patterns (SADPs) of the 49.7 and 79.8 mole% $YO_{1.5}$ specimens, taken tilted a few degrees off a ⟨111⟩ zone axis. Note the considerable amount of diffuse intensity in between the sharp Bragg reflections. While the intensity of this diffuse distribution has diminished in the case of the 79.8 mole% $YO_{1.5}$ specimen, the general form is apparently identical on either side of the two-phase region.

oscillation photographs. However, backscattered electron images of the same material showed that two compositions were coherently intergrown on a micrometer scale, such that the ~100 μm single crystals were a composite of the two end member compositions. The other two compositions within the two-phase region (57.9 and 73.0 mole% $YO_{1.5}$) also showed intimate intergrowths of the end members, but it was not possible to analyze within discrete domains.

The range of the two-phase region based on the various microprobe data is estimated at 55.0 to 74.1 mole% $YO_{1.5}$, possibly as wide as 50.5 to 76.6 mole% $YO_{1.5}$ if we accept that the domain size was not always large enough to permit analysis of a single end member. This range compares reasonably well with the XRD derived range 49.6 to 73.3 mole% $YO_{1.5}$. Both results indicate a broader two-phase region than found by previous investigators, ~55 to 70 mole% $YO_{1.5}$ (4) and ~58 to 72 mole% $YO_{1.5}$ (14).

SINGLE CRYSTAL REFINEMENT RESULTS

The least-squares refinement was performed using full matrix methods minimizing the function $\Sigma w(|F_o| - |F_c|)^2$ where the final $w = [\sigma^2(F) + cF^2]^{-1}$ with $\sigma^2(F)$ obtained from counting statistics and the coefficient c included to give a more realistic distribution of weighted residuals squared. Initially c was set at 0.0016 but was reduced to 0.0004 during the course of refinement.

For the 79.8 mole% $YO_{1.5}$ crystal the $Ia\bar{3}$ parent positions of $YO_{1.5}$ were used as the initial starting model while for the other structures the 79.8 mole% $YO_{1.5}$ final solution was used. The high symmetry metal site R(1) was refined with isotropic thermal parameters, whereas the low symmetry metal site R(2) had anisotropic thermal parameters. Likewise O(1) was anisotropic and O(2) isotropic, except for the 49.7 mole% $YO_{1.5}$ where O(1) was constrained to be isotropic.

Since the 16(c) site (~1/8 ~1/8 ~1/8) was only partially occupied, with especially low occupancy in the C-type structures, the overall thermal parameter $(U_{11} + U_{22} + U_{33})/3$ was coupled to that of the other oxygen, except for the 49.7 mole% $YO_{1.5}$ where this thermal parameter was refined independently. The resulting effect on the thermal parameters of the 48(e) oxygens is small as there are at least 12 times as many oxygens in the 48(e) sites.

Data with $I > 3\sigma(I)$ were refined for several cycles, at which time an empirical absorption correction using second and fourth order spherical harmonic terms was applied to correct for poor crystal shape. The presence of crystal domains which did not contribute to the measured intensity as well as the very irregular crystal shape precluded the application of an independent absorption correction. After further refinement data equivalents were merged to correct for variations induced by the absorption effects that could not be modelled by the empirical correction. Data merging resulted in a reduction of R_1 (for definition see Table 3) by up to a factor of 0.4. Merging was necessary since intensities of equivalents varied by up to 20%. Refinement was complete when there was no further reduction in the goodness of fit and refinement statistics

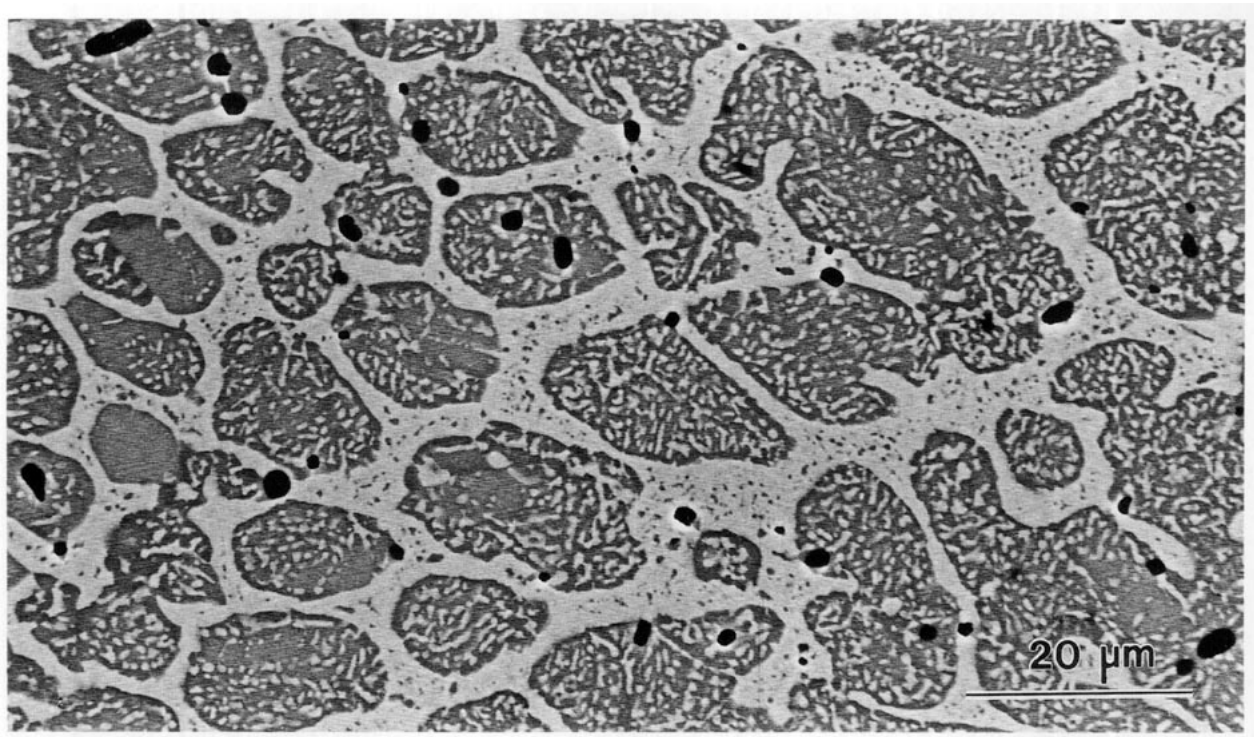

FIG. 4. A backscattered electron image of the 64.8 mole% $YO_{1.5}$ specimen. The intensity is proportional to the average atomic number $\bar{Z}$. The darker regions are the ~73 mole% $YO_{1.5}$ phase and the lighter regions are ~50 mole% $YO_{1.5}$. The sample has unmixed on the micrometer scale.

and the parameter values had stablilized. Because of matrix modification in the constrained refinement errors may be underestimated by a factor of 2.

Nonrandom distribution of Ce and Y atoms between the R(1) and R(2) sites would contribute directly to intensity in the second harmonic (h, k, l; h, k, l even) reflections. Such a nonrandom distribution would, therefore, be most likely for the 79.8 mole% $YO_{1.5}$ specimen as this data set had the most observable second harmonics. However, it should be noted that such compositional modulation is not the only potential contributor to intensity in these second harmonic reflections, and hence their observation need not necessarily imply metal atom ordering.

After merging there were 15 observed second harmonics for the 79.8 mole% $YO_{1.5}$ structure, whereas there was only one such observed reflection for the other two compositions. For the 79.8 mole% $YO_{1.5}$ structure, however, no metal atom ordering was observed. It was, therefore, assumed for the 49.7 and 73.0 mole% $YO_{1.5}$ data sets that no metal atom ordering occurred due to the significantly less observable second harmonic reflections. For these two data sets this parameter was therefore set to zero and not refined.

As the space group $Ia\bar{3}$ has $m3$ point group diffraction symmetry, the possibility of hkl:khl twinning has to be considered, such that the quantity $Y(hkl)$ defined below is the most appropriate description of the observed intensity:

$$Y(hkl) = (1 - \alpha)|F(hkl)|^2 + \alpha|F(khl)|^2.$$

Such a twin ratio parameter α was included in the refinement. After the final cycle it had refined to 0.40(5), 0.13(1), and 0.47(2) for the 49.7, 73.0, and 79.8 mole% $YO_{1.5}$ specimens respectively. This twin ratio was found to have correlation problems in some circumstances.

On completion of refinements the models were checked by resetting of parameters to neutral positions or to the "other side" of the ideal fluorite-type position to ensure no false minima were reached. Solutions were subsequently checked for chemical plausibility by the calculation of bond valence sums, or apparent valences (AVs) (15, 16) for the atom sites.

Crystallographic data for each of the three structures determined, namely, 49.7, 73.0, and 79.8 mole% $YO_{1.5}$ are presented in Table 2. Refinement statistics for the various data subsets are presented in Table 3.

The atomic coordinates and thermal parameters are presented in Tables 4 and 5 respectively. Parameters which were not refined are indicated. The R(2) metal atom displacement, $-R(2)_x$, is plotted as a function of composition in Fig. 5. The AVs have been calculated for the three final refined structures as well as C-type Y_2O_3 and these are presented in Table 6.

79.8 mole% $YO_{1.5}$

The 79.8 mole% $YO_{1.5}$ is within the C-type solid solution. The crystal quality and high number of observed

TABLE 2
Summary of Crystallographic Data

Formula	$Ce_{0.5}Y_{0.5}O_{1.75}$	$Ce_{0.27}Y_{0.73}O_{1.635}$	$Ce_{0.2}Y_{0.8}O_{1.60}$
MW	142.51	128.89	124.75
Unit cell $a_C = b_c = c_C$ (Å) [diffractometer]	10.757	10.698	10.678
Volume	1244.7(3)	1223.3(3)	1217.5(3)
D_{calc}	6.084	5.667	5.420
$F(000)$	2000	1835	1731
Reflections calculated (after merge)	1480 (40)	1432 (44)	2216 (80)
Reflections refined (after merge)	1300 (29)	1252 (25)	1975 (72)
Initial absorption correction type	Spherical radius 0.01 mm	None	Spherical radius 0.02 mm
Absorption correction transmission coefficient range	0.6167–0.6183	na	0.3563–0.3630
Linear absorption coefficient μ[Mo$K\bar{\alpha}$] (calculated) (mm)	32.80	35.61	35.80
Variables after merge	15	19	20
Goodness of fit	3.2661	1.0029	1.0947

TABLE 3
Refinement Statistics for Data Types

Formula	$Ce_{0.5}Y_{0.5}O_{1.75}$	$Ce_{0.27}Y_{0.73}O_{1.635}$	$Ce_{0.2}Y_{0.8}O_{1.60}$
R-factor[a] [refined]	0.0841 (29)	0.0146 (25)	0.0202 (72)
R-factor [calculated]	0.1347 (40)	0.0894 (44)	0.0405 (80)
R-factor [parent]	0.0866 (7)	0.0164 (7)	0.0129 (10)
R-factor [1st harmonics ≥ 1/2 observed]	0.0663 (13)	0.0086 (11)	0.0205 (46)
R-factor [1st harmonics 1/4–1/2 observed]	0.0993 (8)	0.0118 (5)	0.0612 (1)
R-factor [1st harmonics 1/6–1/4 observed]	0.3948 (6)	0.0214 (1)	
R-factor [1st harmonics < 1/6 observed]	0.3976 (3)	0.3179 (16)	0.4451 (3)
R-factor [2nd harmonics ≥ 1/2 observed]			0.0473 (12)
R-factor [2nd harmonics 1/4–1/2 observed]			0.0511 (3)
R-factor [2nd harmonics 1/6–1/4 observed]			0.5606 (1)
R-factor [2nd harmonics < 1/6 observed]	0.0748 (1)	0.0359 (1)	0.3608 (3)

Note. The numbers in brackets are the number of reflections of this type upon which the statistic is calculated.

[a] *R*-factor = $R_1 = \Sigma_h \Delta F(h)/\Sigma_h |F_{obs}(h)|$.

TABLE 4
Refined Atomic Coordinates

	x/a	*y/b*	*z/c*	*x*	*y*	*z*
			⟨(a) 49.7 mole% $YO_{1.5}$⟩			
R(1)	—	—	—	—	—	—
R(2)	−0.0126(13)	—	—	−0.136(14)	—	—
O(1)	0.3780(64)	0.1309(57)	0.3824(72)	4.066(69)	1.408(62)	4.133(78)
O(2)	0.1319(88)	0.1319(88)	0.1319(88)	1.418(95)	1.418(95)	1.418(95)
			⟨(b) 73.0 mole% $YO_{1.5}$⟩			
R(1)	—	—	—	—	—	—
R(2)	−0.0270(5)	—	—	−0.289(6)	—	—
O(1)	0.3868(22)	0.1394(21)	0.3933(22)	4.138(23)	1.491(22)	4.207(23)
O(2)	0.1259(101)	0.1259(101)	0.1259(101)	1.347(108)	1.347(108)	1.347(108)
			⟨(c) 79.8 mole% $YO_{1.5}$⟩			
R(1)	—	—	—	—	—	—
R(2)	−0.0250(2)	—	—	−0.267(2)	—	—
O(1)	0.3861(6)	0.1492(7)	0.3784(7)	4.122(7)	1.593(8)	4.041(7)
O(2)	0.1061(39)	0.1061(39)	0.1061(39)	1.133(42)	1.133(42)	1.133(42)

Note. The positions of the unrefined parameters correspond to the parent positions previously listed.

data, especially second harmonic reflections, resulted in a reliable refinement (R_1 = 0.0202) with low standard deviations on the refined parameters. The results are presented in Tables 2–5. The R(2) Δx, and the O(1) Δx, Δy, and Δz parameters are all consistently less than the corresponding parameters for C-type $YO_{1.5}$. The average position for the O(2) atom site, which is only 20% occupied, appears to deviate from the parent $x/a = y/b = z/c$ = 0.125 position to 0.1061(39).

Initial attempts at refinement used all data equivalents which had at least one observation, however, the comparative refinement statistics (Table 3) show that reflections with less than 1/4 of the equivalents observed have poor refinement statistics and these data calculated low and were subsequently excluded from the refinement.

Given that there is a ratio of metal atom R(1) : R(2) sites of 1 : 3 and a Ce : Y ratio of 1 : 4, Ce might have been expected to occupy R(1) and Y to occupy R(2). For this reason we tested for metal atom ordering. However, refinement of an occupancy parameter, which was initially set at 0.2 for Y on the R(2) site, corresponding to random occupancy, refined to a value of 0.23(1). Therefore we concluded that, within experimental error, there was no evidence for metal atom ordering at this composition.

73.0 mole% $YO_{1.5}$

The 73.0 mole% $YO_{1.5}$ specimen was grown just within the two-phase region, but was nonetheless, to a good approximation, a single crystal. The model refined to R_1 = 0.0146 and the result is presented in Tables 2–5. For reasons given under Experimental, there was no attempt to refine metal atom ordering. A false refinement minimum occurred when $\Delta O(1)_x$ had the opposite sign but AVs showed that this solution was implausible.

49.7 mole% $YO_{1.5}$

The 49.7 mole% $YO_{1.5}$ specimen was in the fluorite-type solid solution. The parameters and refinement statistics are presented in Tables 2–5. When the 79.8 mole% $YO_{1.5}$ refined model was used as a starting model in this refinement, with U_{11} of R(1) > U_{11} of R(2), it was found that the thermal parameters converged to an unrealistic solution. A more plausible solution was obtained when the refinement was constrained such that U_{11} of R(1) < U_{11} of R(2).

Inspection of the refinement statistics suggest a reduced data quality relative to the previous two compositions. It is clear that we were at the limit of information content since first harmonic satellite reflections were substantially weaker and this is reflected in the uncertainties of the refined parameters.

It can be seen in Table 3 that the refinement statistics of the first harmonic reflections in which half or more of the equivalents are observed are better than those of the parent reflections. An attempt was made to introduce two scales into the refinement procedure but the resulting refinement was poorly behaved, with correlations between parameters (e.g., the twin parameter and the O(2) parameter).

The large thermal parameter U_{33} of R(2) corresponds to a mean deviation of 0.38 Å along the z direction from the refined site. An attempt to model this with split atoms

TABLE 5
Thermal Parameters

	U_{11}	U_{22}	U_{33}	U_{12}	U_{13}	U_{23}	U_{eq}[a]
			⟨(a) 49.7 mole% $YO_{1.5}$⟩				
R(1)	0.048(23)	0.048(23)	0.048(23)	−0.024(6)	−0.024(6)	−0.024(6)	0.048(23)
R(2)	−0.002(11)	−0.020(16)	0.143(20)	—	—	−0.080(7)	0.040(6)
O(1)	0.049(32)	0.049(32)	0.049(32)	—	—	—	0.049(32)
O(2)	0.003(59)	0.003(59)	0.003(59)	—	—	—	0.003(59)
			⟨(b) 73.0 mole% $YO_{1.5}$				
R(1)	0.016(5)	0.016(5)	0.016(5)	0.008(2)	0.008(2)	0.008(2)	0.016(5)
R(2)	0.024(3)	0.028(5)	0.016(5)	—	—	−0.011(2)	0.023(2)
O(1)	0.049(24)	0.072(28)	−0.003(14)	−0.034(14)	−0.065(15)	0.043(15)	0.039(7)
O(2)	0.039(7)	0.039(7)	0.039(7)	—	—	—	0.039(7)
			⟨(c) 79.8 mole% $YO_{1.5}$⟩				
R(1)	0.026(2)	0.026(2)	0.026(2)	0.011(1)	0.011(1)	0.011(1)	0.026(2)
R(2)	0.015(1)	0.017(1)	0.003(1)	—	—	−0.004(1)	0.012(1)
O(1)	0.011(5)	0.030(5)	0.013(5)	−0.011(4)	0.006(4)	−0.007(4)	0.018(2)
O(2)	0.018(2)	0.018(2)	0.018(2)	—	—	—	0.018(2)

[a] $U_{eq} = (U_{11} + U_{22} + U_{33})/3$.

failed. This thermal parameter is difficult to interpret in terms of the average structure, but could well be an indication of disorder on the local scale.

Modulation Wave Parameters

When the displacement parameters are calculated in terms of modulation wave (epsilon) parameters the results obtained are presented in Table 7. Due to the large errors the only meaningful nonzero values are the ε_R values for all compositions, the ε'_O parameter for the 73.0 and 79.8 mole% $YO_{1.5}$ compositions, and the ε_O parameter for the 79.8 mole% $YO_{1.5}$ specimen.

There is an apparent discontinuity between the structures on either side of the two-phase region. In the fluorite-type solid solution ε_R ($\equiv -R(2)_x$) is below the expected displacement if it was related to composition by a linear function (the line indicated in Fig. 5). For the C-type solid solution the 73.0 mole% $YO_{1.5}$ displacement is more than that of the 79.8 mole% $YO_{1.5}$. No meaningful comment can be made concerning the other parameters due to the large uncertainties.

The nonzero displacements of ε_R indicate that metal atom shifts are essential in obtaining successful refinements. Thus any model involving only oxygen atom shifts, such as that proposed by Suzuki *et al.* (6–8), can be ruled out.

DISCUSSION

C-type Parent Structure

In the C-type Y_2O_3 parent structure ($Ia\bar{3}$) there are two distinct metal atom sites; the 8(*b*) high symmetry site R(1) and the lower symmetry 24(*d*) site R(2). Figure 6 shows the geometry of the R(1) and R(2) sites and the vacancy distribution with respect to the fluorite parent structure. Both R(1) and R(2) sites are 6-coordinate, but differ in the distribution of the two neighboring vacant anion sites. A metal atom in the R(1) site is surrounded by a $1/2\langle 111\rangle_F$ oxygen vacancy pair, whereas a metal atom in the R(2) site is surrounded by a $1/2\langle 110\rangle_F$ oxygen vacancy pair. For the R(2) site the metal atom is repelled by each vacancy, such that the resultant sum of these displacements is in the $-x$ direction. For the R(1) site these effects cancel and there is no resulting atomic shift.

In the CeO_2-$YO_{1.5}$ solid solutions, as we move from pure Y_2O_3 oxygen atoms are necessarily added to the

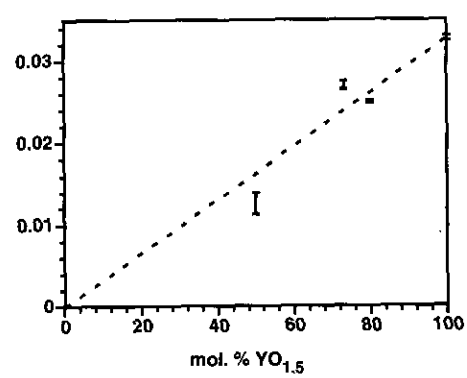

FIG. 5. Plot of the metal atom displacement parameter $-R(2)_x$ as a function of composition. The C-type Y_2O_3 structure parameter is from O'Connor and Valentine (15). The error bars correspond to one standard deviation. The dashed lines on the plot joins the end member CeO_2 and Y_2O_3 values.

TABLE 6
Apparent Valences

	49.7 mole%		73.0 mole%		79.8 mole%		Parent[a] (100 mole%)	
R(1)	Ce	Y	Ce	Y	Ce	Y	Ce	Y
[6]	2.45	2.36	1.97	1.89	3.12	3.01	2.79	2.68
[7]	2.77	2.66	2.09	2.01	3.16	3.04	3.25	3.13
[8]	3.08	2.96	2.22	2.13	3.20	3.08	3.71	3.58
R(2)								
[6]	2.90	2.80	3.20	3.08	2.84	2.74		
[7]	3.06	2.95	3.27	3.15	2.92	2.82		
[8]	3.22	3.10	3.34	3.22	3.00	2.89		
O(1)								
0 Ce	1.79		1.86		1.87		1.79	
1 Ce	1.81		1.87		1.89		1.81	
2 Ce	1.83		1.89		1.91		1.83	
3 Ce	1.85		1.91		1.93		1.85	
O(2)								
0 Ce	1.51		1.22		1.33			
1 Ce	1.53		1.23		1.34			
2 Ce	1.55		1.24		1.35			

Note. Numbers in square brackets indicate the coordination number of the metal atom site.

[a] O'Connor and Valentine (15).

16(*c*) sites. As $Ia\bar{3}$ space group symmetry is preserved for the C-type solid solution these extra oxygen atoms must be randomly distributed. If we add an extra oxygen to either of the vacancies surrounding the R(1) or R(2) sites, both sites become 7-coordinate. For the R(2) site the magnitude of the metal atom displacement will decrease and it will now be directed away from the remaining vacancy. For the R(1) site there will now be a displacement of the metal atom away from the remaining vacancy, the same as for R(2). The effect on the metal atom parameters, compared with C-type, should be that the $R(2)_x$ displacement will decrease and for R(1) there will be an increase in the mean square displacement along ⟨111⟩, i.e., $(U_{12} + U_{13} + U_{23})/3$. As more oxygen vacancies are filled there will be a number of 8-coordinate sites formed. For these sites there should be no displacement from the ideal fluorite position. We would therefore expect that as we move from pure Y_2O_3 to pure CeO_2, there would be an initial increase in the mean square displacement for both R(1) and R(2), but as the composition becomes Ce-rich the mean square displacement for both atoms would decrease as the concentration of 7-coordinate sites becomes small. Unfortunately the standard deviations of the thermal parameters were too large to allow verification of this hypothesis.

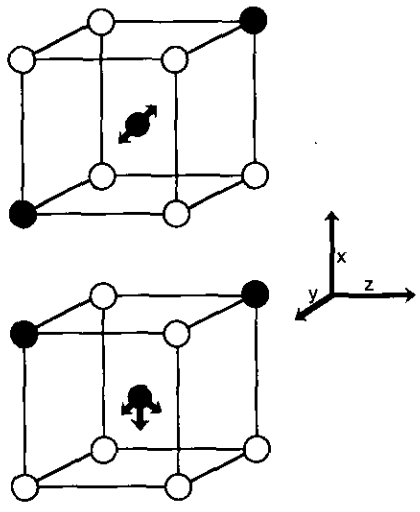

FIG. 6. Shows the R(1) (upper) and R(2) (lower) metal atom sites in C-type. Open circles represent oxygen atoms, the filled circles are oxygen vacancies with smaller shaded circles the metal atoms. The arrows show the direction of repulsion of the metal atom from the oxygen vacancies. For the R(1) site the repulsions cancel whereas for the R(2) site there is a net repulsion in the $-x$ direction.

As one of the primary objectives of this study was to understand in crystal chemical terms the origin of the two-phase region, it is of interest to look for discontinuities in the atomic parameters as the two solid solutions approach the two-phase region. While we have studied only three compositions within the solid solution and the refined displacive parameters have large standard deviations, the $R(2)_x$ parameter (see Fig. 5) strongly suggests a discontinuity in the average displacement, as the respective solid solutions approach the two-phase region. There are also suggestions of a discontinuity in the oxygen displacement parameters, but these data are significantly less reliable.

Apparent Valences

Shown in Table 6 are the calculated AVs for the three final refined structures and the parent $YO_{1.5}$. The coordination of the metal sites changes from 6- to 7- or 8-coordinate if one or both O(2) sites are occupied and so AVs for all three coordinations are presented.

The nature of the bond length–bond valence relationship requires that atoms in a symmetrical coordination

TABLE 7
Epsilon Parameters

	49.7 mole%	73.0 mole%	79.8 mole%
ε_R	0.0126(13)	0.0270(5)	0.0250(2)
ε_O	0.0013(185)	0.0125(111)	0.0193(40)
ε'_O	0.0045(61)	0.0131(22)	0.0176(7)
ε''_O	0.0017(435)	−0.0099(189)	−0.0063(66)
ε'''_O	−0.0063(181)	−0.0072(157)	0.0093(59)

environment can only increase their bond valence sum by moving from the high symmetry site. Therefore atoms which are overbonded when in their high symmetry position cannot relieve this overbonding, whereas atoms which are underbonded, when in their high symmetry position, can relieve this underbonding by such movement. In our refined structural models, atoms which appear to be underbonded would be able to satisfy their bonding requirements locally by moving off the average structure position. This local displacive disorder should be reflected in the U_{ij} parameters for these underbonded atoms. Statistical errors in the U_{ij} parameters prevented verification of this hypothesis. For model purposes, we therefore deemed underbonded atoms to be acceptable, but substantially overbonded atoms to be unacceptable.

In the 79.8 mole% $YO_{1.5}$ structure the Y atom AVs show the Ce atoms to be underbonded for all coordinations in all metal atom sites. The Y atoms in the R(2) site are slightly underbonded, but in the R(1) site are satisfactorily bonded within error. The O(1) oxygen has an AV of 1.87–1.93 and O(2) an AV of 1.33–1.35, depending on how many Ce and Y atoms to which they are locally coordinated. Therefore, the parameters are deemed acceptable as there is obviously scope for local displacement of these atoms from their refined positions to increase their AV, as discussed above.

For the 73.0 mole% $YO_{1.5}$ the R(1) site is very underbonded for both cations, while the R(2) site is satisfactorily bonded within error. Similar to the 79.8 mole% $YO_{1.5}$, the O(1) site is slightly underbonded, with a site average AV of 1.86–1.91 and O(2) is significantly underbonded with a site average of 1.22–1.24.

In the 49.7 mole% $YO_{1.5}$ the metal atoms are either underbonded or satisfactorily bonded within error, depending on the coordination number. It has AVs for O(1) of 1.79–1.85 and the O(2) AVs are 1.51–1.55, which is a reflection of the greater occupation of this site in the fluorite-type structure than in the C-type structure.

Vacancy Models

Modeling oxygen vacancy distributions has explained many features of complex diffuse X-ray diffraction patterns in fluorite-related ZrO_2–$LnO_{1.5}$ systems (18). The approach used to model the disorder in the fluorite-related structures is to select first the oxygen vacancy distribution, then relax the metal atoms around the vacancies. The rules are to avoid $1/2\langle 100\rangle_F$ and $1/2\langle 110\rangle_F$ oxygen vacancy pairs for all cubes and $1/2\langle 111\rangle_F$ oxygen vacancy pairs across empty cubes.

The C-type Y_2O_3 parent structure, $Ia\bar{3}$, shown in Fig. 7a, has the 16(*c*) sites, i.e., empty O(2) sites, arranged such that there are no $1/2\langle 100\rangle_F$ oxygen vacancy pairs around filled metal atom sites. However, due to the large

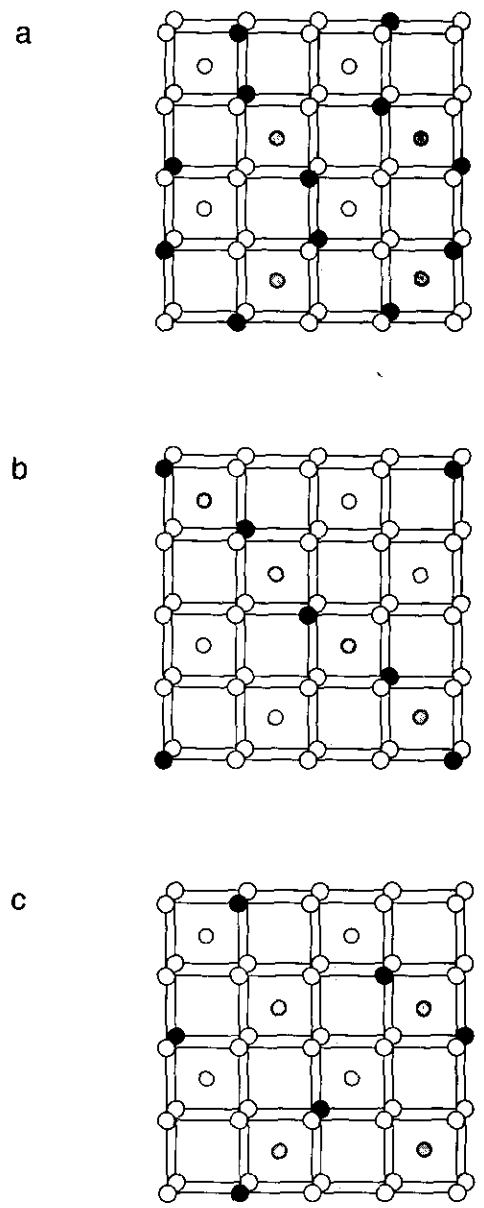

FIG. 7. Quarter unit cell sections of (a) the $Ia\bar{3}$ C-type sesquioxide structure, (b) the $Fd3m$ pyrochlore $A_2B_2O_7$ structure, and (c) the hypothetical $Pa3$ $A_2B_2O_7$ structure. Oxygen vacancies are represented by black circles, *b* is horizontal and *a* vertical. (a) shows a section z = 1/8 to 3/8 in which half of the metal atom sites are R(1) (dark gray) and half R(2) (light gray). The section z = 3/8 to 5/8 (not shown) has only R(2) metal atom sites present. The oxygen vacancies exist as $1/2\langle 111\rangle_F$ or $1/2\langle 110\rangle_F$ vacancy pairs, in filled or unfilled cubes. (b) shows a section $z = -1/8$ to 1/8 in which the metal atoms A (light gray) and B (dark gray) are ordered, with alternate filling of the $\langle 110\rangle$ metal atom chains. The adjacent layers have the *A* and *B* $\langle 110\rangle$ metal atom chains normal to the one shown. Oxygen vacancy pairs exist only as $1/2\langle 111\rangle_F$ pairs around metal atom sites containing the metal atom of smallest atomic radius, i.e., *B*. (c) shows a section z [eq 3/8 to 5/8 of the hypothetical $Pa3$ structure derived from the $Ia\bar{3}$ structure by filling half of the oxygen vacancies. This structure has no $1/2\langle 110\rangle_F$ oxygen vacancy pairs surrounding the R(2) metal atom sites and all the $1/2\langle 111\rangle_F$ oxygen vacancy pairs across empty cubes, leaving all the R(1) metal atom sites as either 6- or 8-coordinate and the R(2) metal atom sites as 7-coordinate.

proportion (25%) of oxygen vacancies, it allows $1/2\langle 110\rangle_F$ vacancy pairs around filled metal atom sites and $1/2\langle 111\rangle_F$ oxygen vacancy pairs across empty cubes.

The fluorite-type solid solution extends to ~50 mole% $LnO_{1.5}$ in ZrO_2–$LnO_{1.5}$ and CeO_2–$LnO_{1.5}$ systems. This is also true of our CeO_2–$YO_{1.5}$ system. If we maintain the same rules as mentioned above, there are only two possible models for accommodating an overall vacancy concentration of 12.5%, corresponding to 50 mole % $YO_{1.5}$, while maintaining overall cubic symmetry in a $2 \times a_F$ superstructure.

One ordered vacancy distribution for 12.5% vacancies already observed is that of pyrochlore $A_2B_2O_7$ ($Fd3m$, face-centered cubic, $a = \sim 10.6$ Å) (19). In pyrochlore the metal atom array consists of rows in the ⟨110⟩ directions, of the A and B cations, that differ in atomic radii by at least 20% (20). A representation of the structure may be seen in Fig. 7b. The $1/2\langle 111\rangle_F$ oxygen vacancy chains are in a zigzag arrangement along the ⟨110⟩ directions, within the cubes containing the cation of lesser radius, i.e., B. The alternate chains have fully occupied oxygen cubes, containing the larger cation, i.e., A. This leaves the metal atom sites as either 6-coordinate for the smaller cations, or 8-coordinate for the larger cations. The vacancies induce repulsion between the adjacent metal atoms, which can only be accommodated because of the smaller atomic radii. This metal atom ordering is incompatible with the $(1 - \delta)CeO_2 \cdot \delta YO_{1.5}$ system as Ce and Y are of the same order of size.

An alternate model for the 12.5% overall vacancy concentration, which has both cubic symmetry and a $2 \times a_F$ superstructure is shown in Fig. 7c. This model has 50% vacancies on the O(2) sites, and fills the vacancies in pairs along the ⟨111⟩ oxygen vacancy strings, i.e., a pair filled, then a pair empty, such that all R(1) sites are either 6- or 8-coordinate and all the R(2) sites 7-coordinate. The ratio of 6 : 7 : 8-coordinate sites is 1 : 6 : 1. This model obeys all the rules for vacancy ordering which have been used successfully in simulating the diffuse intensity distribution in ZrO_2–$LnO_{1.5}$ systems. This ordered vacancy distribution lowers the symmetry from $Ia\bar{3}$ to $Pa3$ symmetry and provides a way of accommodating the most number of discrete vacancy pairs. This $Pa3$ structure would not require metal atom ordering as in pyrochlore.

However, there is no experimental evidence that the space group symmetry is lowered to $Pa3$. This would require the diffraction patterns to contain $\langle 210\rangle_C$ reflections and they are not observed. However, apparent $Ia\bar{3}$ symmetry can be preserved if half the structure has an origin shift of 1/2, 1/2, 1/2, canceling out the extra reflections. These shifts would need to occur on the ~100–300 Å scale.

The 49.7 mole% $YO_{1.5}$ structure is not inconsistent with this model. The only significant deviation from the parent structure is the $R(2)_x$ parameter and the only significant thermal parameter is U_{33} for R(2), which implies a displacement of 0.38 Å in the z direction. The lowering of symmetry to $Pa3$ results in the loss of a two fold axis. This loss allows movement of a metal at R(2) in the y and z directions. The AVs of the new z location of the R(2) are plausible.

The C-type Boundary of the Two-Phase Region

In C-type the parent Y_2O_3 structure has chains of ⟨100⟩ O(1) sites of length 3. This can be seen in Fig. 7a. The distances between these O(1) sites vary from 2.87–3.23 Å and these nonbonded distances all exceed $a/4$ = 2.65 Å, which is the d_{O-O} in the parent structure, i.e., where the oxygen chains have not relaxed toward the vacant sites. Note that in C-type Y_2O_3 the distances between the unfilled 16(c) site and O(1) are 2.37 and 2.50 Å. As a vacancy is filled, two chains of three combine to become a chain of seven (in each of three dimensions), requiring these nonbonded distances to contract which would cause strain within the oxygen sublattice. Further filling of vacancies lengthens the chains and increases the strain until an O(2) site occupancy is reached (about 25% filled for CeO_2–$YO_{1.5}$) at which composition the structure is no longer stable. This O(2) site occupation corresponds to the onset of the two-phase region on the C-type side.

For CeO_2–$LnO_{1.5}$ systems in general, the concentration of $LnO_{1.5}$ at which the two-phase region occurs would depend on the cubic unit cell parameter a, which is a direct function of the size of the Ln cation. The larger the cation, the more oxygens on the O(2) site can be accommodated before the strain, i.e., the nonbonded oxygen distances, become unacceptable. This appears to be validated by the overall trend in the extent of the C-type solid solution in CeO_2–$LnO_{1.5}$ systems (14). In CeO_2–$YbO_{1.5}$ ($a/4 = 2.62$ Å) the solid solution extends to ~93 mole% $YbO_{1.5}$, whereas in CeO_2–$NdO_{1.5}$ ($a/4$ = 2.76 Å) it extends to ~62 mole% $NdO_{1.5}$.

ACKNOWLEDGMENTS

We would like to acknowledge the assistance of Mr. David Vowles and Dr. John D. Fitz Gerald of the Australian National University (ANU) for their help in obtaining EDS analyses and backscattered electron images. Also to Dr. Nick Ware of the Research School of Earth Sciences, ANU for his assistance in collecting EDS microprobe analyses of the samples and Dr. Richard Welberry for stimulating discussions on vacancy modeling and for assistance in generating Fig. 2.

REFERENCES

1. J. D. McCullough, *J. Am. Chem. Soc.* **72,** 1386 (1950).
2. J. D. McCullough and J. D. Britton, *J. Am. Chem. Soc.* **74,** 5225 (1952).

3. G. Brauer and H. Gradinger, *Naturwissenschaften* **38,** 559 (1951).
4. D. J. M. Bevan, W. W. Parker, T. C. Parks, and R. L. Martin *in* "Rare Earth Research" (L. Eyring, Ed.), p. 441. Gordon & Breach, New York, 1965.
5. T. C. Parks and D. J. M. Bevan, *Rev. Chim. Miner.* **10**(1–2), 15 (1973).
6. S. Suzuki, M. Tanaka, and M. Ishigame, *Jpn. J. Appl. Phys.* **24,** 401 (1985).
7. S. Suzuki, M. Tanaka, and M. Ishigame, *J. Phys. C.* **20,** 2963 (1987).
8. S. Suzuki, M. Tanaka, and M. Ishigame, *Jpn. J. Appl. Phys.* **26,** 1983 (1987).
9. R. Wallenberg, R. L. Withers, D. J. M. Bevan, J. G. Thompson, P. Barlow, and B. G. Hyde, *J. Less-Common Met.* **156,** 1 (1989).
10. R. L. Withers, R. Wallenberg, D. J. M. Bevan, J. G. Thompson and B. G. Hyde, *J. Less-Common Met.* **156,** 17 (1989).
11. S. R. Hall, H. D. Flack, and J. M. Stewart, (Eds.), "XTAL3.2 Reference Manual," University of Western Australia. Lamb, Perth, 1992.
12. A. D. Rae, "Raels92," Research School of Chemistry, Australian National University, Canberra, Australia.
13. "International Tales for X-Ray Crystallography," Vol. IV. Kynoch Press, Birmingham, England, 1974 (Present distributor Kluwer Academic, Dordrecht, The Netherlands).
14. D. J. M. Bevan and E. Summerville *in* "Handbook on the Physics and Chemistry of Rare Earths," Vol. 3. (K. A. Gschneider and L. Eyring, Eds.), p. 421. North–Holland, Amsterdam, 1979.
15. H. O'Connor and T. M. Valentine, *Acta Crystallogr. Sect. B* **25,** 2140 (1969).
16. I. D. Brown and D. Altermatt, *Acta Crystallogr. Sect. B* **41,** 244 (1985).
17. M. O'Keeffe, *Struct. Bonding Berlin* **71,** 161 (1989).
18. T. R. Welberry, B. D. Butler, J. G. Thompson, and R. L. Withers, *J. Solid State Chem.* **106,** 461 (1993).
19. B. G. Hyde and S. Andersson, "Inorganic Cyrstal Structures," Wiley, New York, 1989.
20. A. Rouanet, *Rev. Int. Hautes. Temper. Refract.* **8,** 161 (1971).